Surface & Coatings Technology 429 (2022) 127886

Contents lists available at ScienceDirect

Surface & Coatings Technology

journal homepage: www.elsevier.com/locate/surfcoat

Features of ceramic nanoparticle deformation in aerosol deposition explored by molecular dynamics simulation

Bahman Daneshian [a,*], Frank Gärtner [b], Hamid Assadi [c], Maria Villa Vidaller [b], Daniel Höche [a], Thomas Klassen [a,b]

[a] Helmholtz-Zentrum Hereon, Max-Planck-Straße 1, 21502 Geesthacht, Germany
[b] Helmut-Schmidt-University/University of the Federal Armed Forces, Holstenhofweg 85, D-22043 Hamburg, Germany
[c] Brunel University London, Brunel Centre for Advanced Solidification Technology (BCAST) Kingston Ln, Greater London, Uxbridge UB8 3PH, UK

ARTICLE INFO

Keywords:
Aerosol deposition
Cold spray
Nanoparticle
Bonding mechanism
Molecular dynamics

ABSTRACT

The deformation and bonding of particles in Aerosol Deposition (AD) is a topic of growing technological interest for solid-state coating and additive manufacturing with ceramic materials. The core feature of the AD process is the unexpected plasticity of ceramics at high strain rates and small length scales, which is also a topic of general interest for understanding the response of intrinsically brittle materials to dynamic deformation. We explore this feature through computational analysis of the impact of ceramic particles – modelled based on a Lennard-Jones description of submicron TiO_2-anatase particles in a two-dimensional molecular-dynamics system – onto a substrate at a range of impact velocities (100–800 m/s). The deformation behaviour of the particle for each impact velocity was analysed with respect to the evolution of the stress, strain, and temperature fields. The results reveal indications of dislocation-based plasticity within a certain velocity regime. This velocity regime, which becomes narrower with increasing the particle size, coincides incidentally with bonding of particles to the substrate in AD. The results also show that outside this regime, the impact is associated predominantly with either rebounding (at lower velocities) or particle fracture (at higher velocities). The simulation results are interpreted in view of a phenomenological model of fragmentation, considering the interplay between the material properties, such as the fracture energy, and the kinetic energy of particles upon impact. Based on the simulations and the analytical model, a window of deposition is proposed for AD.

1. Introduction

Bulk ceramic materials are brittle and fail without any plastic deformation when subjected to standard deformation conditions at room temperature [1]. However, a number of ceramic materials exhibit a transition to inelastic deformation under quasi-static compression, when the sample size is reduced to submicron dimensions [2–8]. Kendall et al. [3,4] demonstrated already in 1970s that submicron NaCl particles could be deformed inelastically under quasi-static compressive loading. More recently, inelastic deformation under compression at room temperature has also been reported for Al_2O_3 nanoparticles [5,6], TiO_2-anatase nanoparticles [2], MgO nanocubes [7], GaAs micropillars [8] and Si nanoparticles [9]. There are also examples of research that specify the critical size limit below which plasticity could occur [4,10–13].

Submicron ceramic plasticity has been associated with dislocation glide [14] and twinning [15]. There is also evidence for strain hardening and strain-rate hardening of ceramics, e.g., when exposed to shock wave or high strain-rate compression [16–18]. These effects have been attributed to the generation and propagation of micro cracks, dislocation-based plastic deformation, and phase transformations. Moreover, shear localization has been suggested to be a dominant factor in deformation and fracture of fine ceramic powders exposed to relatively high strains (0.2–0.4) and strain rates ($>10^4$ s^{-1}) under compression [20–22]. The inelastic deformation of small ceramic particles can be associated with significant heat release, which could facilitate formation of shear bands [10,11,21,22]. However, the existing interpretations are mostly speculative, and the deformation mechanism for ceramics at high strain rates is yet to be fully understood [19]. Besides, most studies on high strain-rate dynamic deformation of ceramics have focused on powder compaction or deformation of sintered bulk materials.

The development of the aerosol deposition (AD) method [23–28] has thrusted the need for an in-depth understanding of high strain-rate

* Corresponding author at: Institute of Surface Science, Helmholtz-Zentrum Hereon, Max-Planck-Straße 1, 21502 Geesthacht, Germany.
E-mail address: bahman.daneshian@hereon.de (B. Daneshian).

https://doi.org/10.1016/j.surfcoat.2021.127886
Received 10 September 2021; Received in revised form 30 October 2021; Accepted 31 October 2021
Available online 6 November 2021

Abbreviation

AD	aerosol deposition
CS	cold spraying
MD	molecular dynamics
D	dislocation
2-D	2 dimensions

Symbols

a	$=\frac{1}{q}$ in Eq. (14), where q is inelastic heat fraction coefficient, 1
b_1, b_2, b_3	fitting constants in Eq. (11), 1
c_p	heat specific capacity, J Kg^{-1} K^{-1}
d_0	atomic diameter, Å (=0.1 nm)
d_p	particle diameter, m
$\frac{d_p}{d_0}$	normalized particle diameter in schematic model, 1
$d_{(fragmentation)}$	fragmentation diameter, m
E	Young's modulus, Pa
E_k	particle kinetic energy, J
E_{el}	maximum elastic energy of particle, J
E_{def}	inelastic deformation energy, J
E_{Fr_II}	required energy for fracturing mode II, J
F	fitting constants in Eq. (13), 1
fs	10^{-15} s
m	atomic mass, kg
ps	10^{-12} s
q	inelastic heat fraction coefficient in Eq. (10), 1
r	distance between two atoms, Å (=0.1 nm)
r_c	cut off distance in Lennard-Jones potential function, Å (=0.1 nm)
S	crack length, m
$\frac{S}{d_0}$	normalized crack length with atomic diameter, 1
t	thickness of the 2-D model system, m
T	temperature, K
T_m	melting temperature, K
ΔT	temperature difference, K
v_p	particle velocity, ms^{-1}
$v_{threshold}$	threshold velocity
Y	stress at yield/fracture, GPa
ρ	density, kg m^{-3}
γ	surface energy, J m^{-2}
ε	Lennard-Jones parameter, eV
σ	Lennard-Jones parameter, Å (=0.1 nm)
σ_{th}	theoretical strength, GPa

deformation of ceramics. In this method, submicron ceramic particles are accelerated to velocities in the range of 100–600 m/s before impinging the substrate in an evacuated chamber at room temperature [23–28], to form dense layers of ceramic. AD deposits can have superior properties, not achievable by applying liquid state high-temperature thermal spraying methods [28] and be used as protective coatings, base for sensors in electronics and optics, magnetic materials, or as semiconducting functional material for solar energy harvesting. There is experimental evidence that monolithic ceramic particles could show plasticity or pseudo plasticity during AD deposition [26,27].

In terms of the processing principles, the AD method is similar to cold spraying (CS) [29]. In both processes, solid particles at temperatures far below the melting point impinge a substrate at high velocity. The major difference between AD and CS concerns the type of feedstock, i.e., typically submicron ceramic powder for AD and micron-sized metallic powder (usually above 20 μm) for CS. The bonding mechanism of particles in CS is attributed to shear instabilities during plastic deformation of the interacting interfaces between particle and substrate due to local adiabatic temperature rise and the associated thermal softening [29]. Very recent work on AD of copper demonstrated that these concepts also hold for submicron metallic particles [30]. The experimental work on AD has been complemented by theoretical analyses through various numerical modelling methods. Examples include application of finite element method (FEM) [26–27], molecular dynamics (MD) [35–38], smoothed particle hydrodynamics (SPH) [31] and nonlinear transient FEM [39,40] in the study of particle impact in AD. Based on these studies, various bonding mechanisms have been proposed for AD [26–27,31–40]. The main proposed mechanisms are (1) room temperature impact consolidation (RTIC) [26–27,35–40], (2) fragmentation and packing [31], (3) interlocking along with creation of highly activated surfaces [32,33], and (4) 'shear localization' [41]. It is not clear whether and to what extent these explanations, especially the latter, can be applied to intrinsically brittle ceramics particles. The question of deformation and bonding mechanism in AD has thus remained open to a large extent.

The present study aims to address this question, to shed light on the mechanism of AD deposition and in particular, to identify the role of plasticity – be it dislocation glide or shear localization – in particle bonding. In addition, we seek explanations through numerical modelling for nanocrystallisation as observed in AD coatings. The study is based on MD simulations, which has already been widely used for structural and mechanical analysis of ceramic particles. The focus is on TiO_2-anatase – a material of particular interest for photo-catalytic applications [42]. The MD parameters are tuned in such a way so that the tensile properties of the modelled system match the experimentally obtained values of the yield/fracture strength and Young's modulus of anatase [2,43]. The numerical results are analysed with respect to the evolution of the thermomechanical field variables (stress, strain, temperature) and further interpreted in view of a phenomenological model of fragmentation. In this way, the behaviour of particles during AD is predicted and mapped for a range of particle diameters and impact velocities.

2. Methods

The MD simulations were performed by LAMMPS (https://lammps.sandia.gov) software. The following, modified Lennard-Jones potential [38] was applied for the MD simulations:

$$U = \varepsilon\left[\left(\frac{\sigma}{r}\right)^{12} - \left(\frac{\sigma}{r}\right)^{6}\right], r < r_c = 3.345\ \text{Å} \quad (1)$$

where r is the distance between two atoms, r_c is an adjustable cut-off radius, $\sigma = 2.23$ Å is the characteristic length scale (bonding length) and ε is the characteristic energy parameter. Brittleness was introduced by tuning the cut-off radius according to previous work where r_c is set to 3.345 Å, i.e., 1.5 σ [38]. The ε parameter was tuned by tensile and compression MD simulations in order to mimic the brittleness and the compression behaviour of a 33 nm TiO_2-anatase particle for mechanical properties being available from the literature [2,43]. By subsequent fine-tuning, r_c and the ε parameter in Eq. (1) were set to 3.345 Å and 0.45 eV, respectively.

2.1. Tensile test simulations

The 2-D tensile test model setups were made as following: First, the initial atomic configurations of the models were cut out from <10> and <01> crystallographic directions of a close-packed (11) fcc plane in 2-D.

The tensile test in <01> direction model is shown in Fig. 1a. The systems were set to an initial temperature of 300 K. A micro canonical ensemble (NVE) [44] was applied to the tensile test simulations, where the total energy and the volume (area in 2-D) of the simulation system are considered as constant. The time steps were set to 5×10^{-15} s and equations of motion were integrated using the Velocity Verlet algorithm [45]. In the tensile models, one side of the models were considered as fixed and the other side was pulled up with a constant rate of 0.3 m/s in <10> and <01> crystallographic directions. Resulting structures after tensile test simulations and associated stress-strain curves are depicted in Fig. 2. Although both strain modes proof the brittle material behaviour, the stress-strain curves in <10> and <01> crystallographic directions reveal slight differences by anisotropy.

2.2. Compression test simulations

Particle compression simulations were initially designed in order to tune the Lennard-Jones potential to reflect the experimentally determined mechanical properties of TiO_2-anatase nanoparticles of similar diameter given in literature [2,43]. The 2-D compression model was created (Fig. 1b) from three parts: (i) a moving rigid upper jaw on the top, (ii) a fixed rigid lower jaw at the bottom and (iii) a 33 nm diameter nanoparticle in the middle being in contact with both jaws. The upper jaw moved down with a constant velocity of 40 m/s due to restricted computational time in MD. All these parts were cut from an atomic (11) fcc plane. The compression tests were performed using a constant energy condition (NVE). The MD algorithms were the same as those applied for the tensile test. The test was used to adjust the ε parameter for finally reaching a compressive strength of 11.11 GPa in compression test simulation, comparable to the experimental data that are available from literature for TiO_2-anatase nanoparticles within a diameter range of 30–40 nm [2,43]. Details of compression test simulation and its results can be found in our previous study [41].

2.3. Impact simulations

For impact simulation, as well a 2-D model was set up (Fig. 1c). This impact model consisted of 10, 25, 33, 50, 75, 100 and 300 nm monolithic or single-crystalline brittle nanoparticles and a rigid substrate. A rigid substrate was used to ensure defined strain rates in the particle, avoiding any influence of substrate properties and boundary conditions. Material properties and brittleness of the particle were induced by using the description of the potential as previously determined from the tensile test and compression simulations with $\sigma = 2.23$ Å, $\varepsilon = 0.45$ eV and $r_c = 3.345$ Å. Similar to the previous models, the atomic configurations of the nanoparticles and the substrate were cut out from the close-packed (11) fcc plane. However, due to the fixed atomic positions of the rigid substrate, such epitaxy should have no influence on particle deformation. Also, the impact simulations were carried out under constant energy condition (NVE). The nanoparticles were introduced at initial velocities of 100–800 m/s before impacting to the rigid substrate at an angle of 90°. The scenarios were calculated in velocity intervals of 100 m/s. The time steps were set to 5×10^{-15} s and the equations of motion were integrated using the Velocity Verlet algorithm. For considering a rigid substrate, the positions of atoms within the substrate were fixed. Nevertheless, their corresponding potentials and forces were calculated throughout the simulation. Stress and local temperature field variables were calculated by LAMMPS (https://lammps.sandia.gov) and the strain fields were separately extracted by using OVITIO version 3.0.0, (www.ovito.org) [46].

3. Results

3.1. Study of deformation mechanism by stress, strain and temperature fields

Representative impact scenarios obtained by the MD simulations and shear strain analysis for TiO_2-anatase particles with a diameter of 33 nm that impact at velocities of 100, 400 and 700 m/s on a rigid substrate are compared in Fig. 3a and b, respectively. In the comparison of Fig. 3a, three distinct impact behaviours can be distinguished as (i) rebounding, (ii) full bonding without fragmentation, and (iii) partial bonding with fragmentation. The rebounding behaviour was observed for impact velocities $v_p < 400$ m/s. For the rebounded particles, the deposition

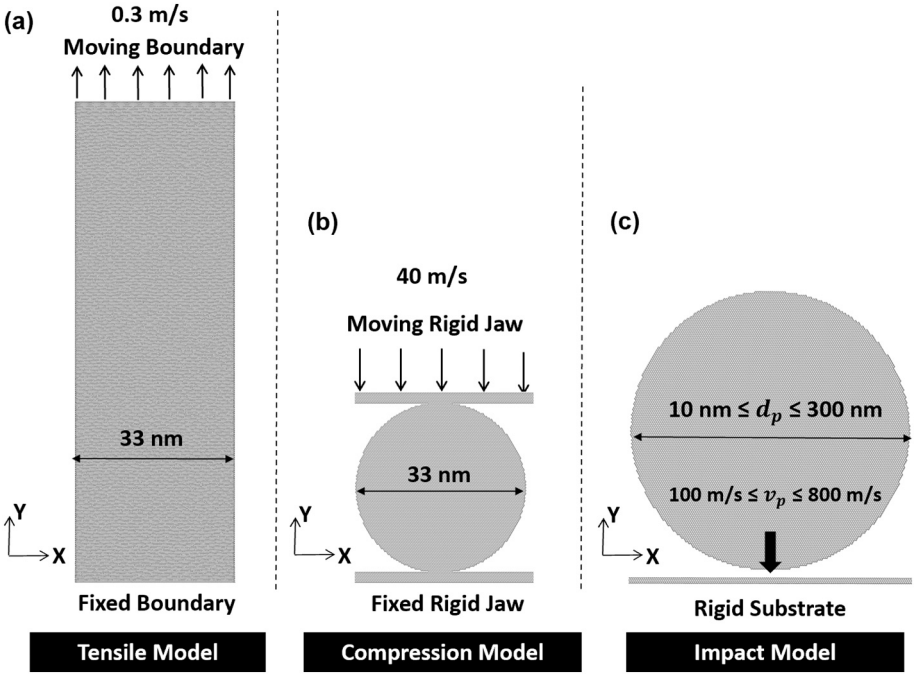

Fig. 1. Main simulation model setups for (a) tensile test simulation, (b) compression test simulation and (c) impact simulations at 100–800 m/s. Particle diameters of 10, 25, 33, 50, 75, 100 and 300 nm were used in the impact modelling. The compression test simulations (b) were used for adjusting the material properties with respect to available results for real TiO_2-anatase from literature [2,43].

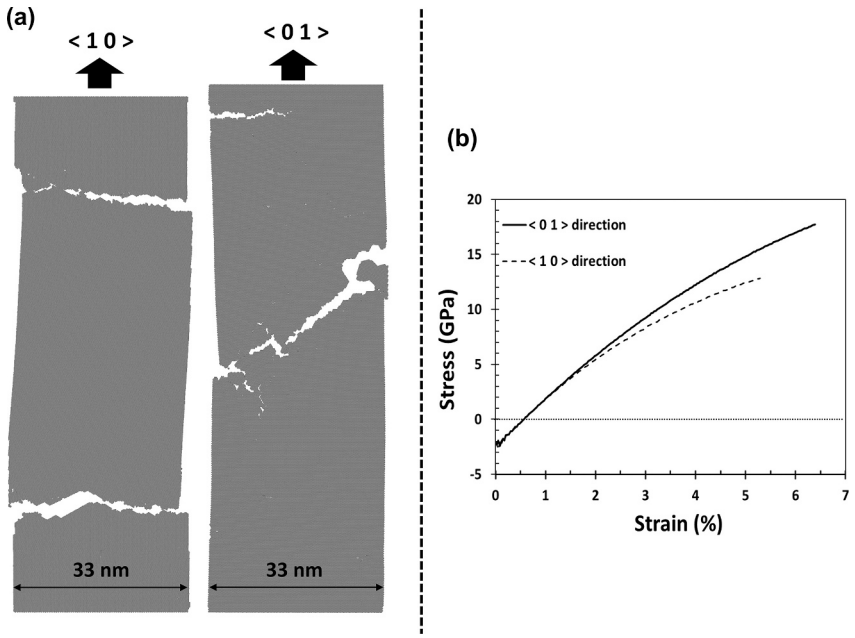

Fig. 2. Results from tensile tests simulations showing (a) the final crack paths fracture in the defect free single crystal tensile test models after application of the tensile loading in <10> and <01> crystallographic directions and (b) resulting stress-strain evaluation.

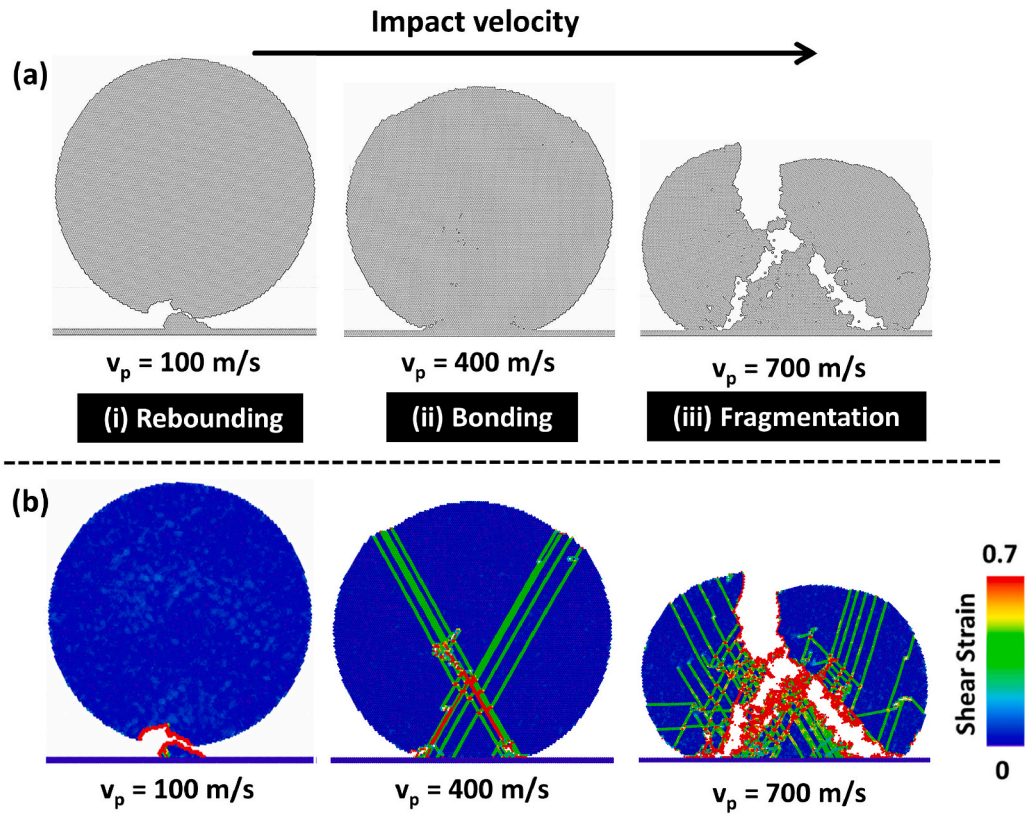

Fig. 3. (a) Calculated impact morphologies (a) of the brittle TiO_2 nanoparticle 33 nm in diameter for impact velocities of 100, 400 and 700 m/s at room temperature as starting conditions. Three typical impact behaviours of (i) rebounding, (ii) full bonding without fragmentation, and (iii) partial bonding with fragmentation are observed. (b) Strain distributions inside the atomic structure of the 33 nm TiO_2 particle after simulation with impact velocities of 100, 400 and 700 m/s, respectively, showing typical examples for the different pattern of rebounding, bonding and fragmentation.

efficiency, here defined as the ratio of atoms in parts adhering to the substrate to the total number of atoms in the particle, reaches less than 10%. Bonding of complete particles was computed for $400 \leq v_p < 600$ m/s. Fragmentation was observed if $v_p \geq 600$ m/s. For the fractured particles, the deposition efficiency, i.e., the ratio of bonded atoms, was around 30% at the lower impact velocities, and decreased with further velocity increase. The three impact behaviours of rebounding, bonding and fragmentation were also obtained, when the particle and the substrate had different initial crystallographic orientations. However, the velocity ranges for obtaining them, were slightly different.

For associating the distinguished impact scenarios given in Fig. 3a with individually different deformation behaviours, Fig. 3b shows the atomic shear strain distributions corresponding to the final states after impact at velocities of 100, 400 and 700 m/s. The dark blue areas

correspond to the elastic regions. The areas coloured in a range from green to red underlie an atomic shear strain of 0.4 to 0.7 that indicates inelastic deformation and plasticity. In general, it can be inferred from this figure that rebounding, e.g., at 100 m/s, corresponds to elastic behaviour, except for the final fracture area close to the interface to the substrate, where some traces of the particle bond to the substrate. At velocities ≥400 m/s, inelastic deformation initiates at the interface to the substrate, and then spreads towards the centre of the particle mostly along with the (11)-slip directions. For velocities ≥600 m/s, inelastic deformation spreads over larger widths, but also shear cracks start to form and to grow. Despite substantial parts of the particle moving to the sides (X-direction) and getting lost by such fracture, a dense cone of highly deformed material remains well bonded in all cases of these high velocity events (v > 600 m/s). The results suggest that these nanoparticles exhibit inelastic deformation for velocities ≥400 m/s. Avoiding rebounding and fracture by deformation features, the velocity regime of 400 to 600 m/s can enable the adhesion of whole particles and might be associated with needed criteria for bonding. However, with respect to continuous bombardment of ceramic materials during AD, also the velocity regimes causing fracture could possibly contribute to layer formation. As main feature, the inelastic deformation appears to play a key role for bonding.

In order to understand the nature of these inelastic deformations, the concept of the von Mises shear strain method applied by OVITO was compared with the concept of one Burger's vector in a 2D closed-packed structure. The shear strain is calculated in 2-D by OVITO [46] from the three components of the atomic strain tensor per Eq. (2), where e_{ij} refers to the atomic strains in X, Y and XY directions. In fact, the shear strain is determined by calculation of the atomic-level deformation gradient and the strain tensor for each atom by the relative motion of its neighbour atoms defined via a cut-off space [47].

$$\text{shear strain} = \sqrt{\left({e_{xy}}^2 + \frac{\left(e_{xx} - e_{yy}\right)^2}{2}\right)} \tag{2}$$

In addition, according to the formal definition of Burger's vector, one step of sliding of atomic planes in a 2D closed-packed structure should result in a value of $\vec{b} = 2\tan(\pi/6) = 1.15$. Such displacement between two adjacent atomic configurations leads to a shear strain value of 0.58. Thus, the green regions in shear strain fields of Fig. 6 and even Fig. 3, correspond to a displacement of one Burger's vector. Therefore, it can be claimed that the inelastic deformation mechanism expressed in the shear strain fields is attributed to plastic deformation.

For gaining an inside view on the atomic structure under more severe deformation, three different areas inside the modelled TiO_2-anatase particle impacting the substrate at a velocity of 400 m/s were displayed with higher resolution at 12.5 ps after first contact when the particle reaches to equilibrium condition in Fig. 4. Fig. 4a shows the front of a spreading dislocation. Fig. 4b shows the interface of the particle to the substrate where most of plastic deformation initiates. Fig. 4c exhibits the intersection of dislocations at the top of the cone shape region spreading from the bottom of the particle. Appling a Burgers analyses to the surrounding of disturbed areas reveals an edge dislocation on the (11)-plane in Fig. 4a during propagation from the particle centre. However, more works is needed to transfer these concepts of plastic deformation from a simplified closed packed 2-D model to real 3-D structures as TiO_2-anatase or others. The static situation in an equilibrated configuration after dislocation emission at the interface to the substrate can be seen in Fig. 4b. For this complex atomic arrangement, it is not possible to perform a detailed Burger's analysis. However, a shear crack and vacancies can be identified as the main defects that remain in the finally relaxed condition within this region. Highest shear strains are observed in the intersection of plastic deformations, as shown in Fig. 4c. Apart from local dislocation like arrangements, slight crystal rotation and disordered areas can be observed.

Fig. 5 reports the cumulative average values of total atomic strain over all atoms in the particle, in X (perpendicular to impact direction), Y (parallel to impact direction) and shear strain for different impact velocities, i.e. v_p. The integration was performed until the end of the simulation in case of shear strain, and until the start of fragmentation inside the particle in cases of X- and Y-strains, respectively. The integrated values were then divided by the number of atoms inside the nanoparticle. The determination of total X- and Y-strain values for velocities larger than 600 m/s was not possible due to particle fragmentation and separation. Below v_p of about 400 m/s, the average value of shear strain shows a linear increase with the impact velocity. Above v_p of about 400 m/s, however, when rebounding behaviour is finished and the bonding behaviour started, a considerable increase in slope of the shear strain curve is observed. At $v_p > 600$ m/s, the slope of shear strain drastically decreases. This could be attributed to fragmented parts not contributing to shear and also not applying loads to the adhering material anymore. Within the rebound range of $v_p < 400$ m/s, the Y-strain is negligibly small and rather constant. At v_p between 400 and 500 m/s corresponding to the bonding regime, Y-strain decreases, by negative values indicating compressive strain nature. The compressive Y-strain is then released at the onset of fragmentation at a v_p of 600 m/s. The X-strain is negligible at small impact velocities of up 200 m/s corresponding to the rebound regime. For higher velocities of up to 500 m/s, already corresponding to the bonding regime, it shows a rather linear increase, indicating growing tensile loads perpendicular to impact direction and associated deformation. At 600 m/s, just before the onset of fragmentation, a drastic rise in X-strain is observed. This indicates that X-strain plays a very important role in fragmentation of the impacted particle at velocities equal and higher than 600 m/s. In summary, the

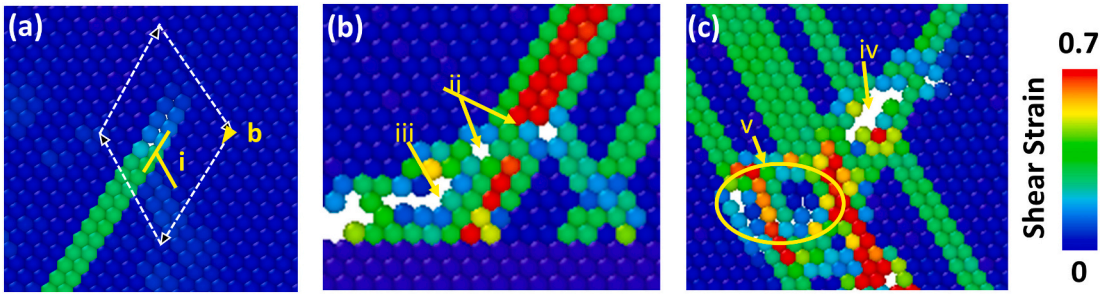

Fig. 4. Details of deformation pattern and strain distribution within the 33 nm TiO_2-anatase particle colliding to the substrate with an impact velocity of 400 m/s at 12.5 ps after first contact when the particle reaches to equilibrium condition. Local atomic arrangements are shown for (a) front of spreading dislocation, with Burgers analyses (i), (b) the interface of the particle to the substrate, where most of plastic deformation initiated, and (c) intersection of dislocations at the top of the cone shape region spreading from the bottom of the particle. The details of deformation features allow the distinction of different defect types as (i) edge dislocation, with burgers vector $\vec{b}$ (i), vacancies (ii), shear crack nuclei (iii), vacancy cluster (iv) as possible crack nuclei, and intersection of dislocations, leaving a distorted area (v).

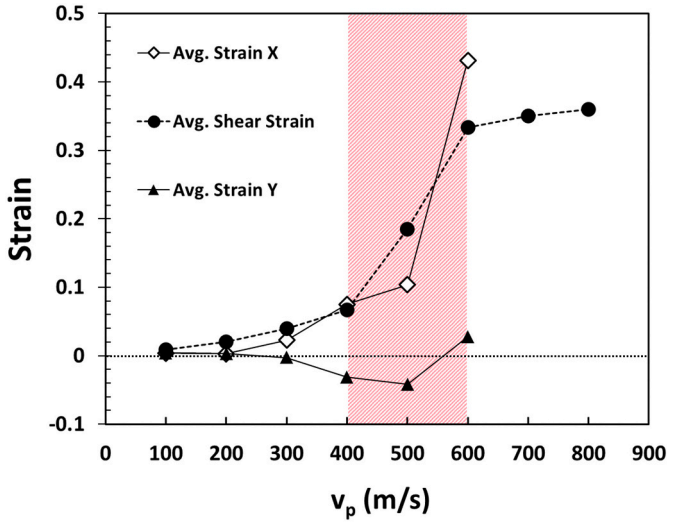

Fig. 5. Average over total, cumulative atomic strains in X- (perpendicular to impact direction), Y- direction (parallel to impact direction), as well as shear strain inside the brittle nanoparticle for a range of different impact velocities of 100–800 m/s. The integrations were performed until the end of the simulation in case of shear strain, and until the start of fragmentation inside the particle in cases of X- and Y-strains and by dividing that by the number of atoms inside the nanoparticle. A considerable increase in slope of the shear strain and strain in X is seen at 400 m/s < vp < 600 m/s (hashed region), which can be attributed to the rise of occurring deformation features and in addition to first occurring internal cracks inside the particle.

comparison of the different strain developments helps to distinguish the influences on particle deformation behaviour. Particularly, the shear strain development directly indicates the velocity regimes for impact behaviours of rebounding, bonding and even fragmentation.

In order to identify the nature of the inelastic deformations, observed in Fig. 3, a combination of subsequent stress, strain and temperature analysis were performed. Fig. 6 exhibits the temporal development of stress in Y-direction (parallel to the impact direction), shear strain, temperature and stress in X-direction (perpendicular to the impact direction) in the 33 nm that shows the bonding behaviour by colliding at an impact velocity of 400 m/s onto the substrate. Time sequences of 3.5, 4, 4.5 and 5 ps after initial contact to the substrate were selected in order to illustrate the initial changes in stress concentration at the contact area, stress releasing, inelastic deformation and temperature evolution. As shown in Fig. 6a, a homogenous stress gradient in Y direction (parallel to the impact direction) develops from the contact point and the maximum stress, localized at the interface to the substrate, reaches up to 32 GPa. Despite the ongoing particle movement and the increase of contact area to the substrate, local compressive stresses show a gradual relaxation with increasing time at 4, 4.5 and 5 ps, respectively. This development cannot be explained just by elastic phenomena. The explanation for the stress pattern development is given by the sequential formation of inelastic deformation as depicted in the shear strain fields in Fig. 6b. From comparing the stress in Y direction in Fig. 6a with the shear strain fields in Fig. 6b, it becomes obvious that this inelastic deformation locally occurs in areas of highest stress, and that local stress release is associated with the formation of such inelastic deformation.

The local temperature evolution at the time sequences of 3.5, 4, 4.5 and 5 ps inside the 33 nm particle is depicted in Fig. 6c via analysing the kinetic energy of atoms in the surrounding of defined atoms. The applied method and its accuracy for calculation of temperature fields has been shown in Fig. 7. The comparison of the evolution of local temperature fields (Fig. 6c) with that of the strain distribution fields (Fig. 6b) reveals that local heat generation is associated with plastic deformation. Even within the investigated short time scales, heat diffusion seems to play a role. The local heat is distributed to regions in the vicinity of originally occurring plastic deformation, finally resulting in a rather uniform temperature distribution.

In addition, comparing shear strain (Fig. 6b) and respective temperature fields (Fig. 6c) at time sequences of 3.5, 4 and 4.5 ps also allows to follow the formation sequence of the plastic deformation fields. According to these figures, the heat is generated upon occurrence of the plastic deformation and then rapidly dissipates to the surrounding. Strain and temperature fields at time sequences of 4 and 4.5 ps reveal the occurrence of second and third sets of dislocations (D_2 and D_3) by the green shear strain fields mainly in the vicinity of previous ones, despite a possible local stress relaxation. The tracked temperature fields allow to determine the exact location of the heat source. For example, D_2 was formed at about the middle of D_1, where the highest initial temperature is observed, and then propagated from there. However, D_3 nucleated like D_1 at the interface to the substrate, but in rather short distance. Judging from stress relaxation reducing local stresses and temperatures at points of origin of secondary plastic deformation events, the results indicated that thermal activation has a major influence in causing consecutive plastic deformation. Fig. 6d shows the stresses in X-direction and reveals high stress concentrations in the centre of the particle at 4.5 ps after initial contact, which then spreads to the upper parts of the particle (see contact time of 5 ps).

Fig. 8 displays the development of stress in Y-direction (Fig. 8a), shear strain (Fig. 8b), temperature (Fig. 8c) and stress in X-direction (Fig. 8d) for the 33 nm particle and the impact velocity of 400 m/s for later time sequences of 5.5, 6, 6.5 and 8.5 ps after initial contact. These sequences were selected in order to illustrate the evolutions in stress relaxation and temperature distribution inside the particle. As shown in Fig. 8a, the Y-stress releases gradually until a time of about 6.0 ps. For longer times (6.5 ps), the decrease in Y-stress speeds up, leading to a rather complete stress release at about 8.5 ps. The reason for this stress relaxation is given by the shear strain development in Fig. 8b, showing spreading plastic deformation and the short sequence of initiating new dislocation sets ones mainly at the cone shape region at the interface of the particle to the substrate. Fig. 8c depicts the corresponding temperature evolution. Highest temperatures are reached in areas of highest shear localization and intersection of plastic deformation fields, here mainly arising in a central area in the lower third volume of the particle. At a time of 8.5 ps, the temperature is still locally higher in the lower cone shape plastic deformation zone of the modelled TiO_2-anatase particle. As illustrated in Fig. 8d, the stress evolution in X direction shows an increase with time, dominating the overall stress states at 5.5 to 8.5 ps. These results indicate that high stresses in X direction can cause formation of possible cracks inside the particle.

The simulations also support the understanding of grain refinement due to plastic deformation. The example in Fig. 9 shows the deformation pattern and local orientational mismatch for a particle impact under non-epitaxial crystallographic orientation to the substrate. The 33 nm TiO_2-anatase particle was first rotated by 30° around its centre and then collided with the substrate at an impact velocity of 500 ms^{-1}. In Fig. 9a, a large angle grain boundary is observed at the bottom part close to the substrate and a low angle grain boundary can be seen at the top-left part of the particle. The rotation field analyses in Fig. 9b - 9d reveal the mismatch with more precision by calculation of the crystallographic rotation matrix and determining regions with different rotation values of 11°, 5° and 3°, respectively. These different range of atomic rotations around Z axis with respect to their initial positions (as reference points) can distinguish between existing low and large angle grain boundaries inside the particle. Particularly the orientation fields in Fig. 9c reveal grain refinement for the more heavily deformed areas close the substrate.

For comparison of the deformation mechanism pattern between ceramics and metals, separate sets of MD simulations were applied to the deformation of a 33 nm copper particle impinging the substrate at a velocity of 600 m/s. As for TiO_2-anatase, the 2D-model was created by a cutting an epitaxial arrangement of substrate and particle out from a

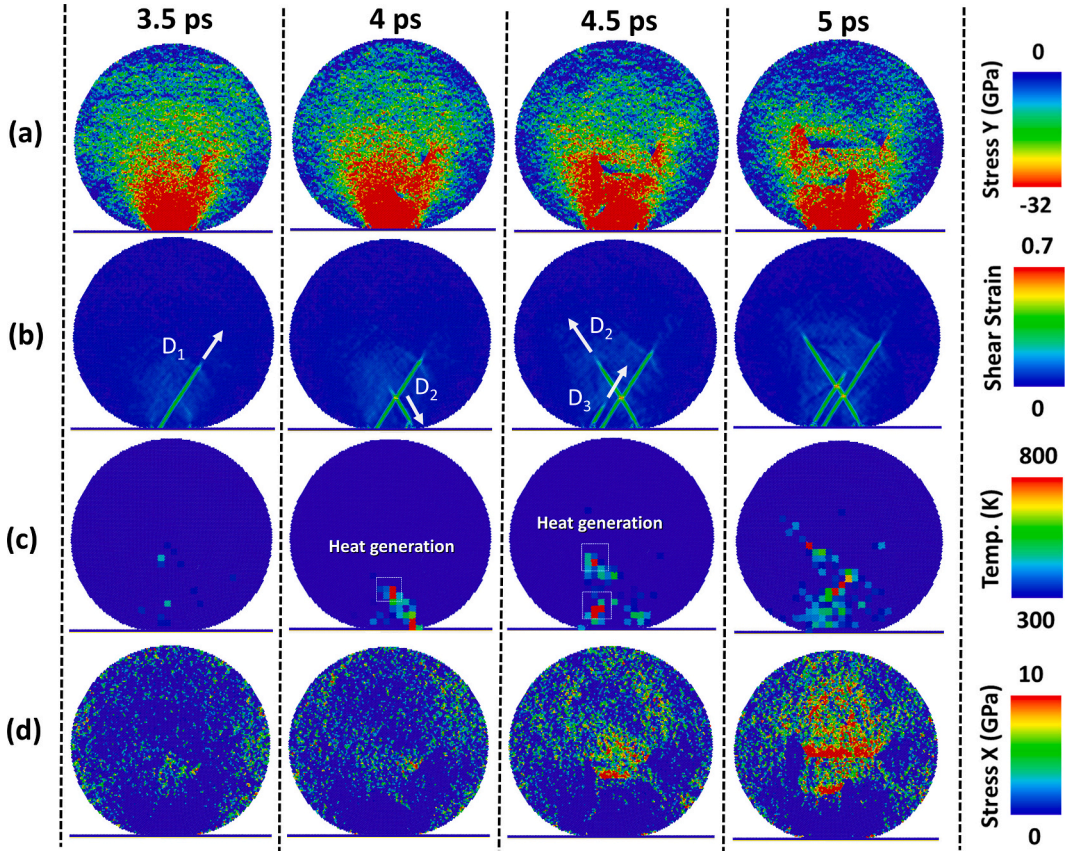

Fig. 6. Temporal development of stress in Y (parallel to the impact direction), shear strain, temperature and stress in X (perpendicular to impact direction) inside the 33 nm TiO_2 particle during impact with a velocity of 400 m/s at 3.5, 4, 4.5 and 5.0 ps after the first contact to the substrate. Stress Y localization (3.5 ps) and local Y-stress release (4–5 PS) can be revealed in (a). Shear strain fields in (b) depict formation sequences of plastic deformation at the lower part of the particle from 3.5 to 5 ps by dislocations, indicated as D_1 to D_3. Heat generation in (c) follows the current moving direction of progressing dislocations in (b). The generated heat (c) dissipates then fast to the surrounding. Stress concentration in X-direction (perpendicular to impact) in (d) indicate tensile forces spreading from the centre to the upper part of the particle.

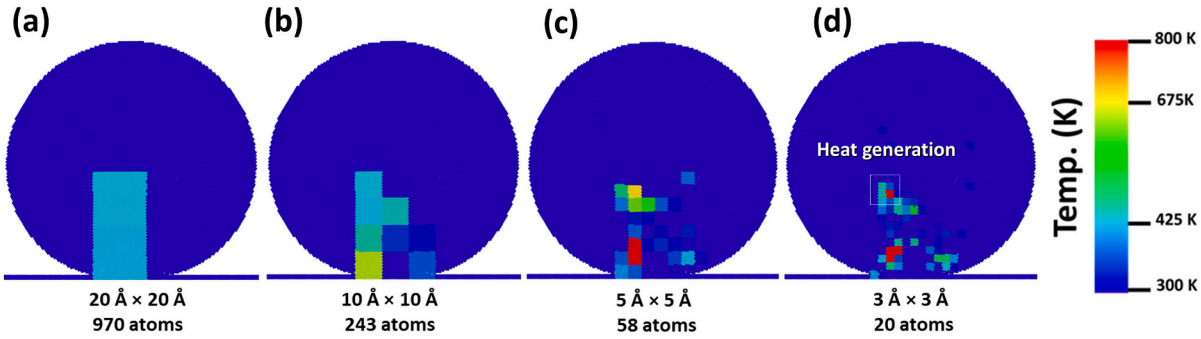

Fig. 7. Influence of different domain (box) sizes (a-d) on accuracy of temperature field measurement for the 33 nm TiO_2 particle during impact with a velocity of 400 m/s. The temperature field was measured in the vicinity of a dislocation (D) in Fig. 6b at 4.5 ps after impact.

(11) plane. The velocity of 600 m/s was selected to allow for a direct comparison to the ranges studied for TiO_2-anatase and for observing features during impact of a small copper particle at maximum velocities reachable by using nitrogen as process gas during AD. For the quantitative description of copper properties, the EAM potential function [48] was used. Fig. 10 shows the atomic shear strain for different time steps and reveals that plastic deformation begins at the interface between the particle and the substrate, and spreads towards particle core (Fig. 10a). Similar to the deformation of a TiO_2-anatase particle at same velocity, regions with high shear strains rapidly spread over more than half of the whole size (Fig. 10b). Showing the shear strain distribution in 3 times larger range than for TiO_2-anatase, areas of highest deformation can be identified, roughly showing similar pattern as obtained for the ceramic material, but here corresponding to up to 3 times higher atomic displacement. The comparison of the result for copper with those shown for the TiO_2-anatase nanoparticle (Figs. 3, 6, 8) at same impact velocity confirm that even at these diameters areas of plastic deformation in metals much more prominently occur than in ceramics. Moreover, the maximum values of local shear strain inside the ceramic are much smaller than that of the metal. For justifying the concept of modelling for the deformation of metals, simulations for copper were also performed using higher impact velocities (the example for 1000 m/s is presented in

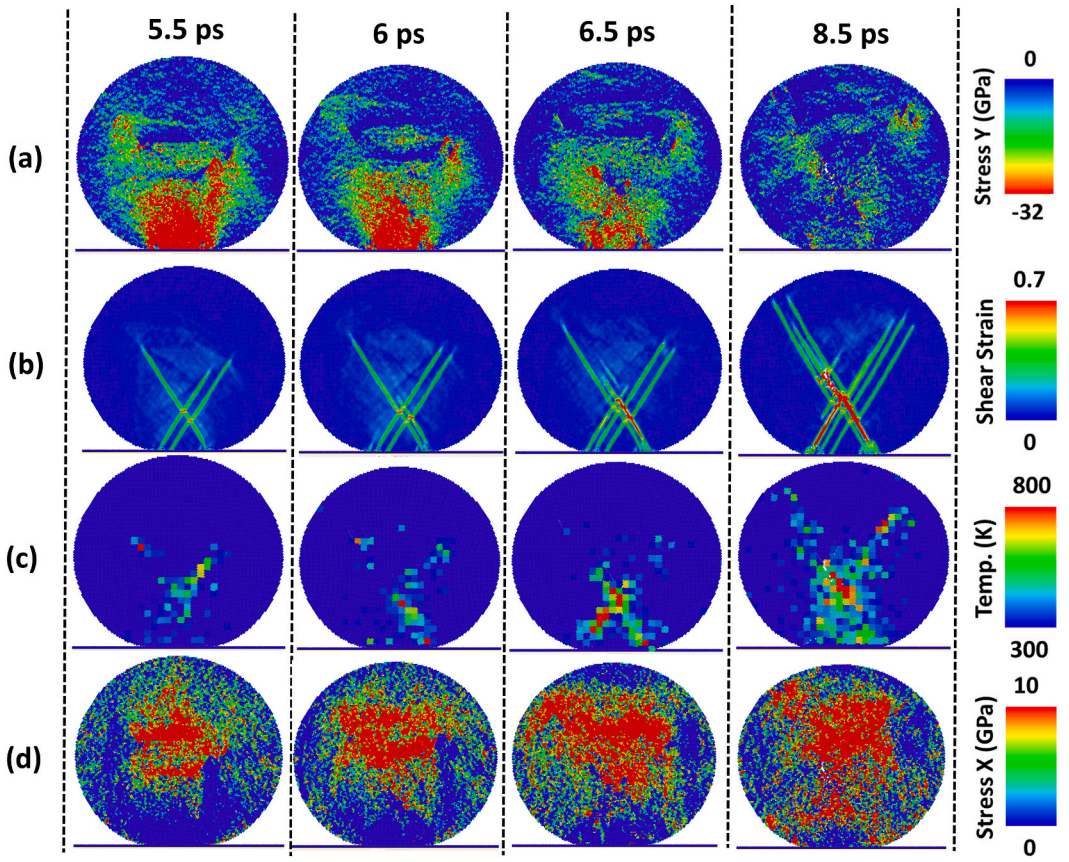

Fig. 8. Temporal development of stress in Y (parallel to the impact direction), shear strain, temperature and stress in X (perpendicular to impact direction) inside the 33 nm TiO_2 particle during impact with a velocity of 400 m/s at 5.5, 6, 6.5 and 8.5 ps after the first contact to the substrate. (a) illustrates the continuing, gradual Y-stress release (5.5–8.5). Shear strain fields in (b) depict formation and progressing of multiple dislocations inside the particle. Local temperature fields in (c) reveal heat generation according to dislocation movement and following heat dissipation. (d) Stress concentration in X direction becomes more dominant and cover larger parts of the upper particle area.

Fig. 11). The results show that sufficiently highly velocities result in similar deformation pattern as observed in FEM analyses or experiments of cold sprayed Cu-particles [29] and rather well agrees to recent results on AD of Cu [30]. Differences with respect to needed velocities are most probably due to size effects and specific modelling approaches (here 2-D).

In addition to the numerical study of deformation features and strain developments, further studies were performed in order to develop an analytical model to explain the observed impact behaviours of rebounding, bonding and fragmentation, as given in the next section.

3.2. Analytical models

The molecular-dynamic simulations revealed that rebounding occurs at low impact velocities, when plastic deformation inside the particle can be neglected - Fig. 3. In addition, extended MD simulations showed that the velocity regime for rebounding is not size dependent [41]. For the present material description of TiO_2-anatase, the maximum rebounding velocity, here defined as threshold velocity, $v_{threshold}$, is determined to 400 m/s for a range of particle diameters from 25 to 300 nm [41]. The bonding behaviour starts as soon thresholds for the activation of plastic deformation are exceeded, thus indicating a velocity dependent brittle to ductile transition. In the following, the threshold velocity and rebounding behaviour are described by analytical methods and compared with the MD simulation results.

3.2.1. Threshold velocity

Judging from the shape of rebounding cracks spreading rather parallel to the interface to the substrate (X-direction in Fig. 3), they might be initiated by tensile stresses when the particle after reaching maximum loads already moves back in reverse direction. These results thus indicate that rebounding is caused by the tensile stress applied in Y-direction to the collided, and now reversing particle. Based on this observation, an analytical model for rebounding of brittle particles can be developed to describe and predict threshold velocities during AD.

Following descriptions for particle rebound in CS [49], rebounding can be distinguished as long as the kinetic energy of the particle E_k, is smaller than the maximum elastic energy, E_{el}, that stores in the particle in Y direction (flight direction) - Eq. (3a).

$$E_k < E_{el} \tag{3a}$$

As soon as the kinetic energy of particle, E_k, exceeds the maximum elastic energy, E_{el}, conditions for bonding are attained. Therefore, the respective border is given by Eq. (3b).

$$E_K = E_{el} \tag{3b}$$

The maximum elastic energy per volume, E_{el} (in Y-direction), can be derived from integrating the stress-strain diagram given in Fig. 2b for the tensile test model (Fig. 1a). By considering the associated numbers of atoms, the results can be transferred to the particle volume in order to obtain the maximum elastic energy stored in the particle before crack formation and rebounding - Eq. (4). The particle volume in 2-D is calculated by considering the particle as a flat cylinder with diameter size d_p and thickness t. The thickness of the 2-D model system corresponds to the atomic diameter, but can be treated as an arbitrary value

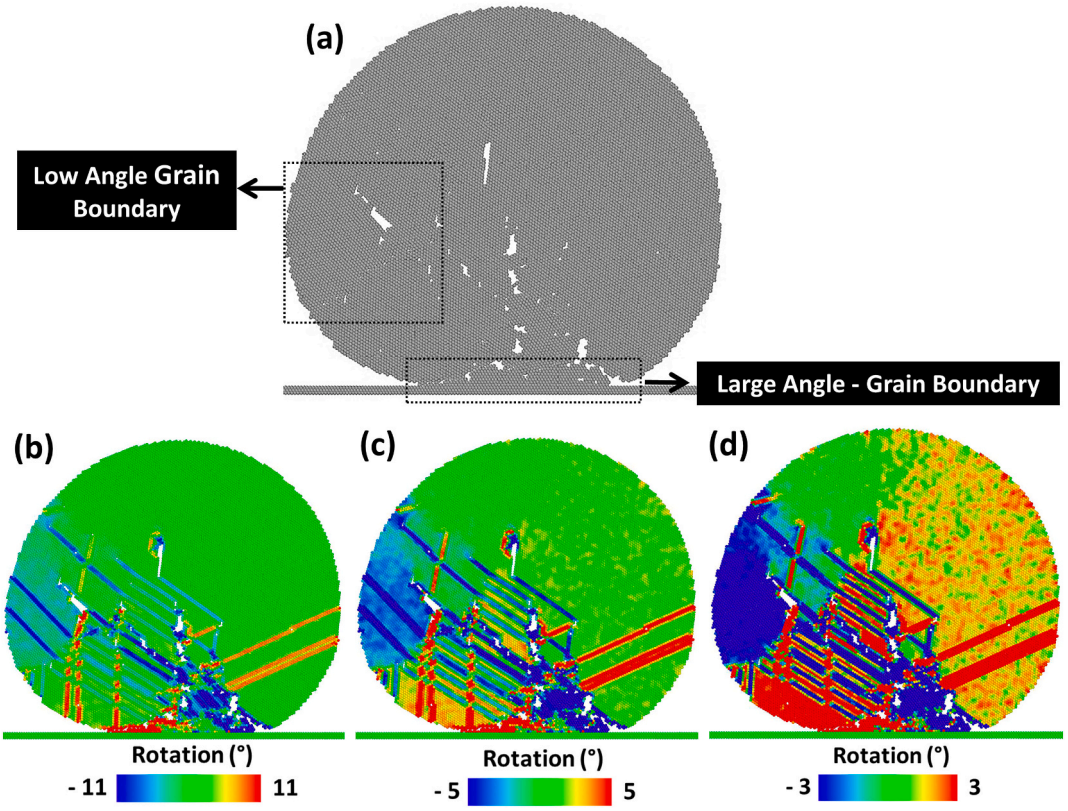

Fig. 9. Deformation features and rotation fields of a non-epitaxial impact at a velocity of 500 m/s of a 33 nm TiO_2-anatase particle, rotated 30° with respect to the substrate. (a) illustrates the impact morphology with cracks and atomic configuration. (b, c, d) illustrate the rotation fields for mismatches of 11, 5 and 3 degrees, respectively. Nanocrystallization is visualized by low and large angle grain boundaries (b, c, d).

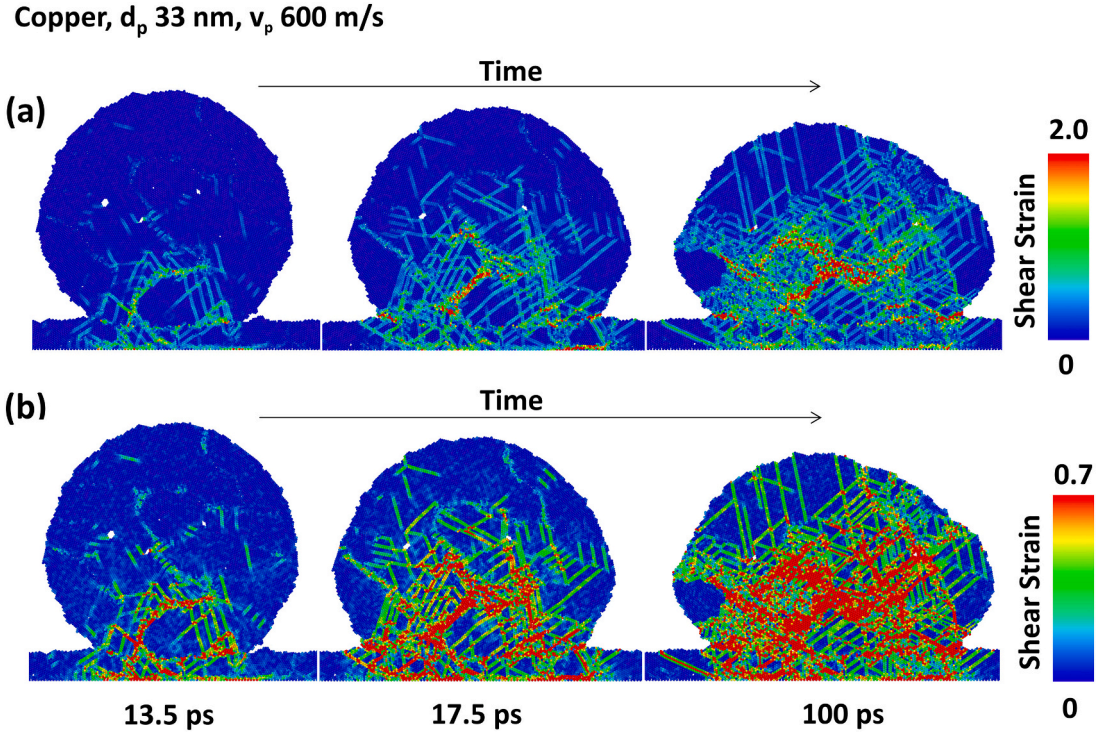

Fig. 10. Snapshots of atomic shear strain for a 33 nm copper nanoparticle impinging the substrate with a velocity of 600 m/s at room temperature for different deformation sequences. The final time of 100 ps corresponds to the time of system equilibration. The different ranges in strain should allow to recognize general features (max. Strain of 3.4 atomic displacements) and a direct comparison to the strain fields occurring in ceramics (strain $\geq$1.2 atomic displacement).

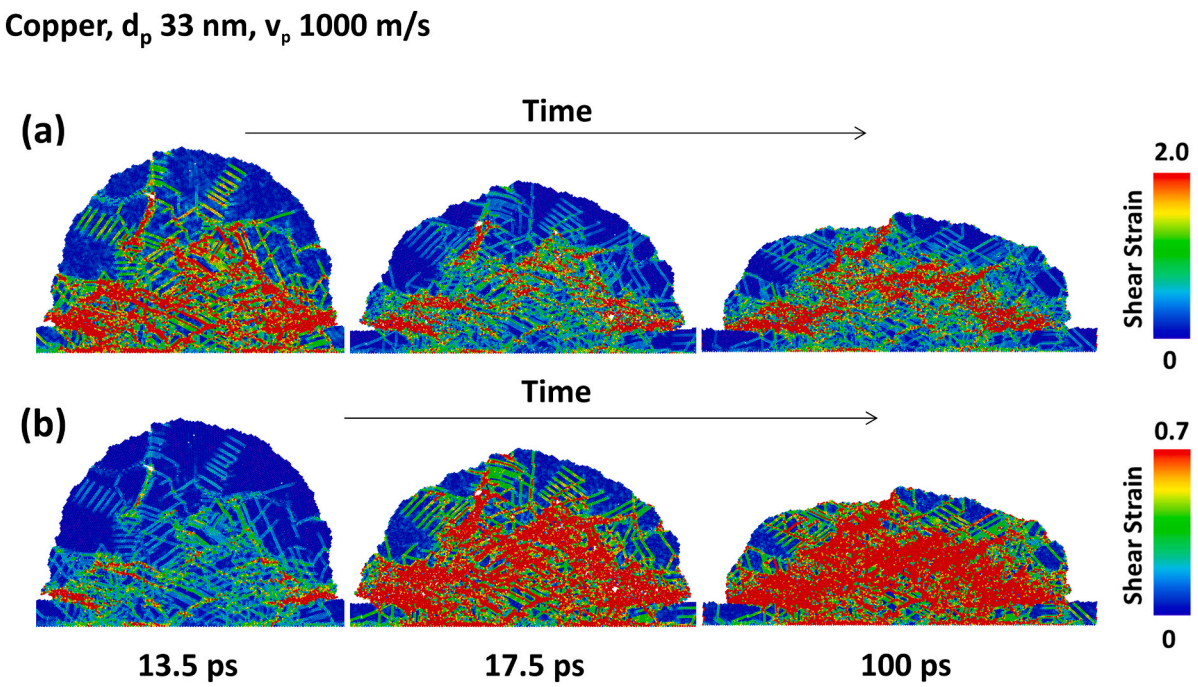

Fig. 11. Atomic shear strain for a 33 nm copper nanoparticle impacting on a rigid substrate at a velocity of 1000 m/s at room temperature. This figure shows the distribution of strain fields inside the particle at large (a) and small (b) atomic shear strain ranges from 0 to 2 and 0–0.7, respectively.

since it can be removed from both sides of the equation. The energy terms in Eq. (3b) can be rewritten in Eqs. (4)–(5) as a function of material properties, particle diameter and particle velocity as following:

$$E_{el} = \frac{m}{\rho}\frac{Y^2}{2E} = \frac{\pi t d_p^2}{8}\frac{Y^2}{E} \tag{4}$$

$$E_k = \frac{1}{2}mv_p^2 = \frac{\pi t d_p^2}{8}\rho v_p^2 \tag{5}$$

where m is mass of the cylindrical particle model in 2-D, as calculated on basis of the particle volume, ρ is density, Y and E are the tensile stress at yield/fracture and the Young's modulus, respectively, as obtained from the MD stress-strain diagram for pulling in Y-direction. Eq. (3b) can then be simplified to Eq. (6) as a size independent formula:

$$v_{threshold} = \sqrt{\frac{Y^2}{\rho E}} \tag{6}$$

Eq. (6) can be solved in order to calculate the threshold velocity ($v_{threshold}$) between rebounding and bonding behaviours. For comparison with the MD simulation results, same model parameters are considered ($\rho = 8980$ kg/m^3). The high density is attributed to the simplification as close packed 2-D monoatomic MD model. The values of Y and E were obtained from tensile test simulations in Y direction to be 17.7 GPa and 277 GPa, respectively (compare Fig. 2b). The high value of Y is due to the lack of any defects inside the initial tensile test model. In fact, the value of Y is comparable with the theoretical strength, i.e., σ_{th}, of the developed TiO_2-anatase model according to an accepted model for ceramics [50]. With these data, the application of Eq. (6) yields a threshold velocity of 355 m/s for the TiO_2-anatase particles, which is in good agreement with the threshold velocity of 400 m/s obtained from the impact simulations.

For supplying an estimate for $v_{threshold}$ based on material data, following assumptions can be made. The stress at yield/fracture of a defect free single crystalline ceramic structure roughly corresponds to the theoretical strength of that material, thus σ_{th}, can be related to the Young's modulus by Eq. (7), as developed for ceramic materials by Davidge et al. [50]. With this relation, Eq. (6) can be rewritten in Eq. (8), now containing the theoretical strength. Such would allow general estimates of the threshold velocity for a wide range of brittle materials.

$$Y = \sigma_{th} \approx \frac{E}{10-20}\ [50] \tag{7}$$

$$v_{threshold} = \sqrt{\frac{{\sigma_{th}}^2}{\rho E}} = \sqrt{\frac{E}{k^2\rho}};\ with\ k = 10\ to\ 20 \tag{8}$$

For testing the model, Eq. (8) was applied to calculate the threshold velocities of typical materials that are applied by AD. For the examples of alumina, SiO_2, and TiO_2- anatase. Table 1 compares estimated threshold velocities with so far published experimental data [51], with setting k = 20 [50]. The estimations meet the experimentally determined threshold velocities [51] for bonding in AD with an accuracy of maximum up to 10%, demonstrating a rather good agreement.

3.2.2. Velocity dependent sizes for fragmentation

An energy-based analysis can also be applied to derive a criterion for the transition from bonding to the fragmentation behaviour. In view of the MD simulations, fragmentation starts when the minimum required energy for fragmentation can be provided by particle kinetic energy as per Eq. (9a), where E_{el} is the maximum elastic energy stored in the

Table 1
Values of density, Young's modulus, theoretical strength and calculated threshold velocities ($v_{threshold}$) for some of the most widely used ceramics in AD like Alumina, SiO_2 and TiO_2- anatase. The theoretical strength was considered as 0.05 of the Young's modulus via considering k = 20 in Eq. (7) based on literature data [50]. The threshold velocity was then calculated by using these values by Eq. (8).

Material	ρ (Kg/m^3)	E (GPa)	Y (GPa)	$v_{threshold}$ (m/s) - Model	v_{thr} (m/s) - Literature
Al_2O_3	3000	215	10.75	423	400 [51]
SiO_2	2170	66.3	3.315	276	300 [51]
TiO_2-anatase	3780	230	11.5	390	Not available

particle in X direction, E_{def} is the plastic deformation energy and E_{Fr_II} is the required fracture energy mode II.

$$E_k > E_{el} + E_{def} + E_{Fr\_II} \tag{9a}$$

The border from bonding to fragmentation can be defined as Eq. (9b).

$$E_k = E_{el} + E_{def} + E_{Fr\_II} \tag{9b}$$

According to the MD simulations, at higher impact velocities, fragmentation, which can be seen in fracture mode II, starts from the top part of the particle in Y, <01>, direction. E_{def} can be correlated to the heat generated during plastic deformation of the nanoparticle [52–54]. Thus, Eq. 10 has been here to calculate the particle plastic deformation energy based on the particle thermal energy. The deformation energy and its conversion to heat neither depends on particle size nor material density, but only on the particle velocity [52–54] (see Fig. 12). This concept provides a relation between particle temperature increase (ΔT) and its initial velocity, as given in Eq. (11) as polynomial of 2nd order to describe the temperature based on the kinetic energy of the whole system [55]. Eqs. (10) and (11) are given as following:

$$E_{def} = \frac{1}{q}\, m\, c_p\, \Delta T = \frac{1}{q}\, \frac{\pi t d_p^2}{4} \rho\, c_p\, \left[T_m f(v_p)\right] \tag{10}$$

with

$$f(v_p) = b_1 v_p^2 + b_2 v_p + b_3 \tag{11}$$

q is a coefficient related to the inelastic heat fraction, and should consider that not all plastic deformation transforms into heat. The melting temperature ($T_m = 2080$ K) and the heat specific capacity $\left(c_p = 120\ {}^{J}/_{kg.K}\right)$ used in this equation were calculated separately by a separate MD simulation for a 33 nm particle by using the same Lennard-Jones parameters as for impact simulations. ΔT is correlated to the melting temperature and particle impact velocity through a fitting function, $f(v_p)$ in Eq. (11), with the resulting fitting parameters, b_1, b_2 and b_3 as 10^{-6}, -2×10^{-4} and 2.42×10^{-2}, respectively, (Fig. 13). The last term, E_{Fr_II}, which is the required fracture energy for creation of two crack surfaces with length S in <01> direction at (11) surface, can be expressed as follows:

$$E_{Fr\_II} = 2St\gamma \tag{12}$$

The analyses of crack lengths in fragmented particles are not simple and straightforward even in 2-D. Thus, based on the fragmentation pattern resulted from the MD simulations, a schematic model had to be developed to study the relationship between the crack length and particle diameter, as sketched in Fig. 14a also considering the fact that cracks typically have fractal shapes [56,57]. Then the Eq. (12) can be rewritten as following:

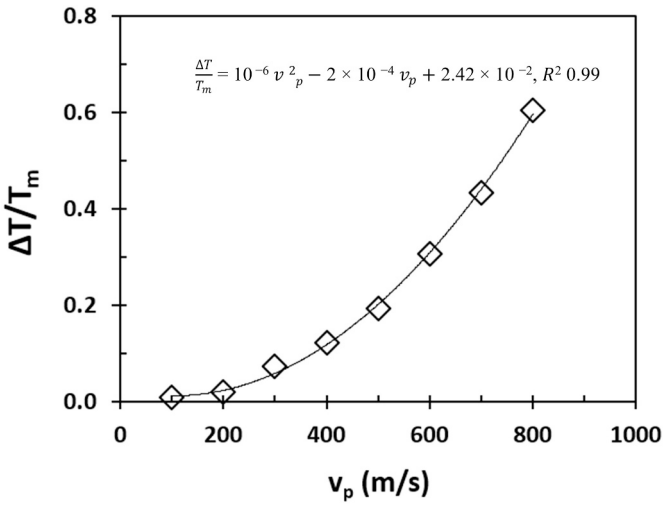

Fig. 13. Normalized temperature changes over impact velocity in the 33 nm TiO_2 particle. The fitting parameters b_1, b_2 and b_3 were applied in the Eq. (11) for a polynomial approximation to the MD simulation data to describe respective correlations.

$$E_{Fr\_II} = 2St\gamma = 2Fd_p t\gamma \tag{13}$$

where F is a fitting parameter estimated to be around 0.71, according to the correlation of Fig. 14b for the assumed simple crack geometry. The required crack surface energy of $\gamma = 2.18$ J.m^{-1} was separately measured by another MD simulation based on a method explained in the literature [38]. Inserting Eqs. (10)–(13) into the Eq. (9b) gives:

$$\pi\left(\rho E v_p^{\,2} - Y^2 - 2aE\rho c_p\, \left[T_m f(v_p)\right]\right) d_p^2 = 16EF\gamma d_p \tag{14}$$

where $a = \frac{1}{q}$. This equation can be used to work out the 'fragmentation diameter', i.e., the maximum particle diameter that shows bonding behaviour with a meridional crack (like Fig. 14a) at a given velocity.

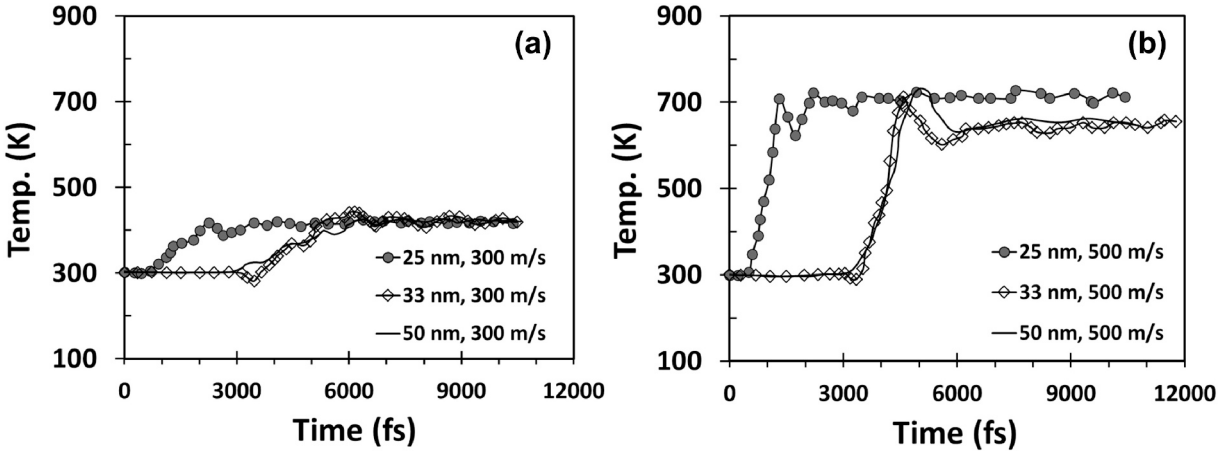

Fig. 12. Developments of mean temperatures of the whole particles over impact duration. In order to apply and to generalize the Eq. (11) for particles of different diameters, it is required to ensure that temperature only depends on the particle impact velocity. These diagrams are presented to confirm this assumption by showing examples for velocities of 300 m/s (a) and 500 m/s (b), where nanoparticles of different diameter show almost similar final temperatures after collision.

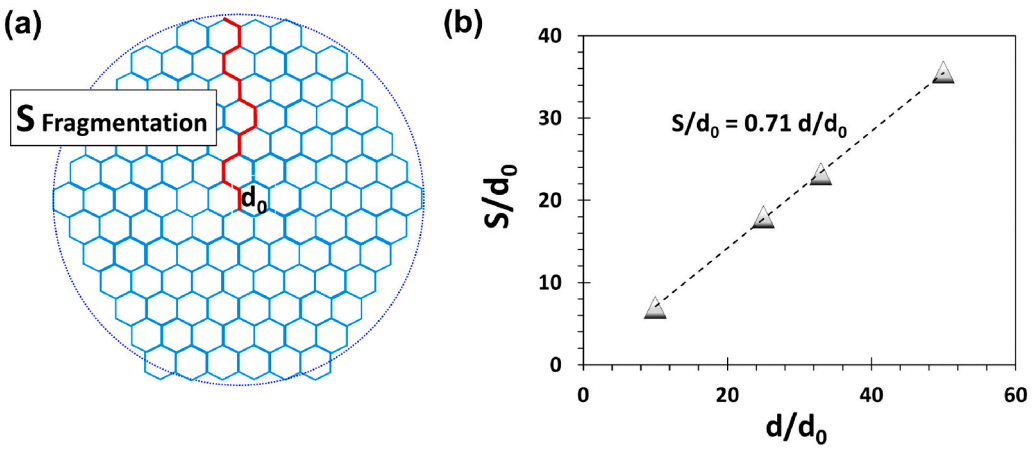

Fig. 14. Schematic for the model of critical crack length approximation and respective correlations with particle diameter in the fragmentation mode. (a) shows a schematic fragmentation crack, and (b) shows the linear relationship between the critical fragmentation crack length and the particle diameter in the presented model.

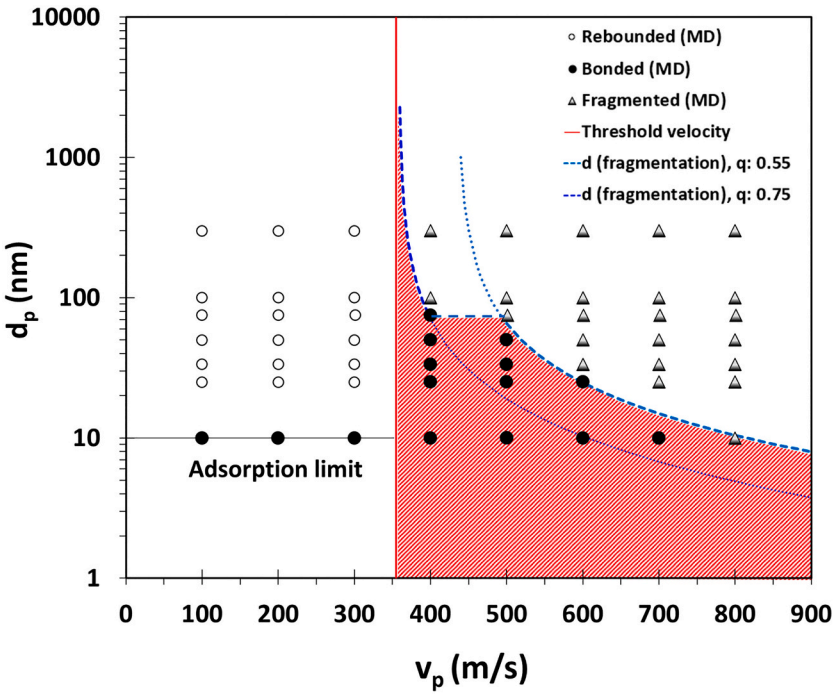

Fig. 15. Regimes for the different deformation modes with respect to particle impact velocity and diameter as window of deposition. The different symbols represent the results from the MD simulations. The red solid line represents the threshold velocity of 355 m/s as given by Eq. (6). The dashed lines represent the transition regime according Eq. (15) between bonding and fragmentation behaviours in the window of deposition. For fragmentation, the best fit with the MD results was attained by considering q = 0.55 in Eq. (15) (light blue dashed / dotted line) at 500 m/s $\leq v_p \leq$ 800 m/s and q = 0.75 (dark blue dashed / dotted line) at $v_p \leq$ 400 m/s. Very small particle with diameter of 10 nm do not exhibit the rebounding behaviour at lower impact velocities. This can be attributed to the adsorption phenomenon due to Van der Waals forces being stronger than rebound stresses by particle kinetic energy. (For interpretation of the references to colour in this figure legend, the reader is referred to the web version of this article.)

$$d_{(fragmentation)} = \frac{16EF\gamma}{\pi\left[\rho E v_p^2 - Y^2 - 2aE\rho c_p T_m f\left(v_p\right)\right]} \tag{15}$$

Since the assumed particle in the fragmentation model contains a meridional crack (Fig. 14a), applying the theoretic strength and related Young's values resulting from tensile test modelling of flawless model in Y or <01> direction (Fig. 2b) in Eqs. (14) and (15) is not accurate. In fact, using these values in Eq. (15) predicts larger particle diameter (d (*fragmentation*)) for the same impact velocity. Therefore, the values of Y and E were obtained from tensile test simulations in X or <10> direction to be 12.8 GPa and 243 GPa, respectively (Fig. 2b).

According to the MD results, at high impact velocities, deformation energy causes internal cracking. At lower impact velocities and near to the threshold velocity, however, internal cracking was not observed. Therefore, quantifying the deformation energy in Eq. (10) in terms of thermal energy via only one uniform value for the 'q' parameter for all impact velocities results in a velocity dependent deviation of the fragmentation model according to Eq. (15) from respective MD results. This can be attributed to particle fragments that do not contribute to a temperature increase of the overall system. This issue can be addressed in the fragmentation model by considering two values of $q = 0.55$ and $q = 0.75$, respectively, for velocity regimes where many or only few fragments are observed. For $q = 0.55$, fragmentation diameters correspond well with the MD results 500 $m/s \leq v_p \leq$ 800 m/s. Similarly, by considering $q = 0.75$, good agreement with the MD results is observed at $v_p = 400$ m/s. This transition in determining the fragmentation diameter by two values for q is represented as dashed lines in Fig. 15.

3.2.3. *Common features from MD simulations and analytical descriptions*

The results of the analytical rebounding and fragmentation models are displayed in Fig. 15 together with the MD simulation results and confirm a good agreement. Both analytical models consistently describe a rather simple way to define a window of deposition predicting particle impact behaviour depending on its size and impact velocity.

Also, as common feature, the borders according to rebounding and fragmentation models' approach each other at 355 m/s, in agreement to simulation results. From this it can be estimated that the bonding behaviour without fragmentation of TiO_2-anatase particles should be most unlikely for larger sizes of some hundreds of nanometers, irrespective of the impact velocity. This means, that possible layer formation of particles larger than that by AD would be always associated with fragmentation.

On the very small particle size regime, the rebound model disagrees to the MD-simulation results. According to the latter, all particles with a diameter of about 10 nm at velocities $< v_{threshold} = 355$ m/s should bond to the substrate. This phenomenon can be attributed to adsorption phenomena. In the MD model, attractive interactions get activated as soon atomic distances fall below the threshold r_c of the modified Lennard Jones model. As long the tensile stress on adjusted bonds is lower than the forces needed to stress the bonds to r_c under the elastic rebound, the particle should bond. The applied tensile stress on the other hand depends on the number of atoms being affected by elastic loads, here in very small particles not reaching the needed thresholds for breaking already existing bonds. In real systems not reaching limits for common grain boundaries, Van der Waals forces might play a similar role with lower interaction energies.

4. Discussion

4.1. Aspects for AD of ceramics

This study for the first time combined applied stress, strain and temperature analysis by MD simulations and analytical models to describe contributions by plastic deformation to bonding phenomena of ceramic nanoparticles under high strain rates at room temperature, here using TiO_2-anatase nanoparticles as model system. The developed models can supply a possible description for AD and contribute to a better understanding of the mechanisms associated with this coating technique. For a particle velocity range of 400–800 m/s, the results revealed the interplay between plastic deformation and fracture as the dominating phenomena leading to either full bonding to the substrate without fragmentation or partial bonding with fragmentation. For velocities smaller than 400 m/s, the particle shows only small amounts of plastic deformation and thus a rebounding behaviour. Strain analysis and deformation pattern demonstrate that the occurrence of plastic deformation by reducing the elastic rebound stresses could enforce bonding between the nanoparticle and the substrate. As shown by subsequent analyses for a wide range of velocities, it seems that the combination of highly localized stress, plastic deformation and associated temperature rise are key factors in high velocity nanoparticle deformation, and probably bonding.

Unlike to previous computer modelling attempts [27,31,35–38,39,40], a wide range of different particle diameters and also velocities were covered in this study to provide a window of deposition. In addition, analytical techniques like stress, strain and especially temperature field analysis were applied to shed more light into individual mechanisms, not being available so far in the previously presented modelling attempts for AD [27,31,35–38,39,40]. However, the major difference to previous simulations [27,31,35–38,39,40] concerns the possibility to reveal plastic deformation in brittle nanoparticles and distributions of respective strain fields. Apart from that, the present simulations can also explain nanocrystallization during AD, as reported by experimental observations [25,58–60], by the rearrangement of local structures by plastic deformation leading to an angular mismatch.

The good consistence between MD simulation results and the description of the particle behaviour by analytical models could enable the transfer of the model to other materials. This would allow to predict the impact behaviour with respect to the impact velocities, particle diameters and respective material properties. For AD, this might enhance a forecast for the ability of a material to form a dedicated coating layer. Nevertheless, due to the simplified 2-D approach used here, the transfer to real systems and particle diameters might need some scaling functions.

Owing to the limitation of computation time in MD, the MD simulations of this study are limited to particle diameters of maximum 300 nm. However, the presented analytical models are not inherently limited to the nanosized particles. For example, the threshold velocity is described by a size independent model. However, a size dependence is then considered in the model for fragmentation. According to that, at the lower border to the threshold velocity, particles with sizes of up to about 2 μm should be able to be bonded without fragmentation. However, in the fragmentation model, the maximum sizes of fully bonded particle then decrease with increasing velocity, as given in Fig. 15. This finding from the fragmentation model is in good agreement with experimental results for AD of TiO_2-anatase powders where particles of up to 2.4 μm in size could be successfully deposited [61,62]. Comparing results of the fragmentation model with the experimental observations, it seems that bonding by plasticity plays an important role for successful deposition of TiO_2-anatase powders via AD. The fragmentation of larger particles and decreasing size boundaries with increasing velocities do not in disagree with experimental observations as long parts of the fragments well adhere to the substrate. Such is ensured by the highly deformed cone areas in the lower particle parts close to the substrate. Indeed, coating processed by AD show internal particle fragmentation and low deposition efficiencies. Thus, layer formation at particles sizes of about 1 μm or more is probably governed by fragmentation, in good agreement to the presented models.

For complete layer build up in real systems, deformation caused by following particle impacts to initial ones have to be considered. Such additional loads would enhance fracture and contribute to the removal of substantial amounts of bonded material. Such might result to features where only parts of the highly deformed and probably grain refined but crack free cone zones of particles are left on the substrate. Possibly remaining nano-crystalline layers would be in agreement to experimental observations for AD [28,58–60].

4.2. General aspects for extracting deformation features of ceramics in AD

The following points address the most relevant field variables to be extracted to reveal deformation features in brittle materials. The basic ideas could probably be applied to other process techniques and strain rates and thus enhance modelling applications for ceramics in general.

4.2.1. Strain distributions, plastic deformation and nanocrystallization

The combination of stress and strain analysis proved as most powerful tool to study the impact behaviour of nanoparticles for a wide variety of impact velocities. For the present study, the average shear strain parameter by the occurring higher amounts of plastic deformation could clearly distinguish conditions within impacted nanoparticle for full bonding from those for rebounding. In addition, the strain in X (perpendicular) direction could separate the fragmentation from the bonding behaviour by a sharp increase of slop at velocities where fragmentation starts.

Strain analysis could also clearly reveal locations of plastic deformations inside the nanoparticle. These regions are observed by shear strain fields within the fully or partially bonded nanoparticles, when the measured local stress at the particle/substrate reaches levels typically being higher than the particle maximum compression strength. These regions of localized plastic deformation then spread to inside the particle along the slip system directions and are accompanied with a release of local stresses and a rise in local temperature. Burgers analyses could reveal dislocation like features. Obtained deformation pattern with locally concentrated plastic deformation and deformation free zones in between have some similarity to shear band like structures observed during the deformation of metallic glasses [63] or composite materials

[64]. At areas of intersecting plastic deformation, a slight crystal rotation could be observed.

Strain analysis also revealed that formation of nanocrystals inside the bonded particles (with or without fragmentation) is related to the localized plastic deformation and respective intersections inside the nanoparticle, as proven by calculating the atomic rotation parameter along with the atomic strain parameter in MD. This could explain nanocrystallization, usually observed in AD [24,26–28], by deformation features. As shown here for the example of copper, the developed strategies for analysing particle impact could be transferred to other materials and possibly also other phenomena.

4.2.2. Temperature distributions

Temperature analysis was performed by calculating the total temperature of the particle as well as monitoring the temperature fields inside the particle during impact simulations in Figs. 6, 8. The comparison between strain fields and local temperatures revealed that the heat is locally generated by plastic deformation. With plastic deformation mainly occurring within a deformation cone between the contact area to the substrate and intersections about the lower third of particle axis, the heat distribution is far less concentrated than in CS, where the high amounts of heat are generated by the deformation at the interface between the particle and substrate. By small dimensions and short diffusion paths, however the heat is distributed over a significant part of the nanoparticle and contributes to an overall temperature rise. Reasons for thermal heat dissipation being more prominent in smaller particles than in larger ones are known from cold gas spraying [52]. This can be attributed to the fact that heat diffusion spreads with the square root of time, whereas the deformation shows a linear correlation. Thus, the heat generation upon dynamic deformation of ceramic nanoparticles is not adiabatic. However, according to our recent MD simulation for larger particles [41], the local temperature of particles with diameters of 300 nm or probably larger can rise locally up to 1200 K, which should be sufficient to support layer formation. Fracture of larger particle can hinder dissipation of the heat to lost parts and thus retains the high temperature inside the remaining cone region on the substrate and might support bonding of following particles in AD [41].

The comparison of shear strain and temperature fields show that regions with higher temperatures support initiating plastic deformation. However, in AD of ceramics, the degree of deformation and thus possible thermal activation of plasticity occurs in lower amount and much less localized to the interface than in CS of metallic particles. Nevertheless, also for the impact of ceramic particles in AD, the plastic deformation remains localized to a highly deformed, and possibly grain refined cone at the lower part of the particles. Locally higher temperatures thus could support the thermal activation of plastic deformation phenomena.

5. Conclusions

By using modelling approaches, the high velocity brittle nanoparticle deformation in AD could be associated with plastic deformation. Three different phenomena as rebounding, bonding and fragmentation can be distinguished, whereas bonding and fragmentation may contribute to coating formation. Governing the occurrence of these phenomena, plastic deformation can be identified as major mechanism enabling bonding and layer formation in AD. Studies of stress, strain and temperature analysis at atomic scale reveal that plastic deformation within the particle initiates at the interfaces to the substrate and then spreads into its centre. It can also be shown that a locally higher concentration of shear and plastic deformation could contribute to grain refinement inside the nanoparticle upon impact.

The transitions between the different phenomena are described by respective analytical models. Energy balances explain the behaviours of nanoparticles upon impact, considering their size, velocity as well as their physical and mechanical properties. These models describe threshold and fragmentation diameters and by that, in agreement to the MD simulation results, define a consistent window of deposition with respect to particle size and velocity. The simulations and the models suggest a maximum fragmentation diameter, above which particle fragmentation in TiO_2-anatase is inevitable. The simplification to a 2-D model and respective simple crystallographic structures may limit the direct comparison to experimentally observed structures and scales. Nevertheless, the general features and trends in any case will hold as suitable description. The developed procedures can also be applied to more sophisticated 3D calculations systems and probably other deformation techniques. Thus, the present work just can be regarded as a first step for consecutive studies to apply MD for processing of ceramics.

Funding

The authors gratefully acknowledge financial support by the Federal Ministry of Education and Research of Germany, in the framework of the Project “FocusH2’’ (No.03SF0479A).

Declaration of competing interest

Maria Villa Vidaller reports financial support was provided by young investigator research group FOCUS H2 (No. 03SF0479).

Acknowledgements

We wish to thank the teams from the Institute of Materials Technology at Helmut Schmidt University and the Institute of Materials Research at Hereon.

References

[1] C.A. Tracy, A compression test for high strength ceramics, J. Test. Eval. 15 (1987) 14–19.
[2] V. Swamy, A.Y. Kuznetsov, L.S. Dubrovinsky, A. Kurnosov, V.B. Prakapenka, Unusual compression behavior of anatase TiO_2 nanocrystals, Phys. Rev. Lett. 103 (2009), 075505.
[3] K. Kendall, Transition between cohesive and interfacial failure in a laminate, P. Roy. Soc. A-Math. Phy. 344 (1975) 287–302.
[4] K. Kendall, The impossibility of comminuting small particles by compression, Nature 272 (1978) 710.
[5] E. Calvié, L. Joly-Pottuz, C. Esnouf, P. Clément, V. Garnier, J. Chevalier, Y. Jorand, A. Malchère, T. Epicier, K. Masenelli-Varlot, Real time TEM observation of alumina ceramic nano-particles during compression, J. Eur. Ceram. 32 (2012) 2067–2071.
[6] E. Calvié, J. Réthoré, L. Joly-Pottuz, S. Meille, J. Chevalier, V. Garnier, Y. Jorand, C. Esnouf, T. Epicier, J.B. Quirk, Mechanical behavior law of ceramic nanoparticles from transmission electron microscopy in situ nano-compression tests, Mater. Lett. 119 (2014) 107–110.
[7] I. Issa, J. Amodeo, J. Réthoré, L. Joly-Pottuz, C. Esnouf, J. Morthomas, M. Perez, J. Chevalier, K. Masenelli-Varlot, In situ investigation of MgO nanocube deformation at room temperature, Acta Mater. 86 (2015) 295–304.
[8] F. Östlund, P.R. Howie, R. Ghisleni, S. Korte, K. Leifer, W.J. Clegg, J. Michler, Ductile - brittle transition in micropillar compression of GaAs at room temperature, Philos. Mag. 91 (2011) 1190–1199.
[9] W. Kang, M.T.A. Saif, In situ study of size and temperature dependent brittle-to-ductile transition in single crystal silicon, Adv. Funct. Mater. 23 (2013) 713–719.
[10] C.J. Shih, M.A. Meyers, V.F. Nesterenko, High-strain-rate deformation of granular silicon carbide, Acta Mater. 46 (1998) 4037–4065.
[11] C.J. Shih, V.F. Nesterenko, M.A. Meyers, High-strain-rate deformation and comminution of silicon carbide, J. Appl. Phys. 83 (1998) 4660–4671.
[12] J. Michler, K. Wasmer, S. Meier, F. Ostlund, K. Leifer, Plastic deformation of gallium arsenide micropillars under uniaxial compression at room temperature, Appl. Phys. Lett. 90 (2007), 043123.
[13] F. Östlund, K. Rzepiejewska-Malyska, K. Leifer, L.M. Hale, Y. Tang, R. Ballarini, W. W. Gerberich, J. Michler, Brittle-to-ductile transition in uniaxial compression of silicon pillars at room temperature, Adv. Funct. Mater. 19 (2009) 2439–2444.
[14] P. Sarobol, M. Chandross, J.D. Carroll, W.M. Mook, D.C. Bufford, B.L. Boyce, K. Hattar, P.G. Kotula, A.C. Hall, Room temperature deformation mechanisms of alumina particles observed from in situ micro-compression and atomistic simulations, J. Therm. Spray Technol. 25 (2016) 82–93.
[15] Y. Hong, N. Zhang, M., Asle zaeem, metastable phase transformation and deformation twinning induced hardening-stiffening mechanism in compression of silicon nanoparticles, Acta Mater. 145 (2018) 8–18.
[16] D.E. Grady, Shock-wave compression of brittle solids, Mechanics 29 (1998) 181–203.
[17] G. Ravichandran, G. Subhash, A micromechanical model for high strain rate behavior of ceramics, Int. J. Solids Struct. 32 (1995) 2627–2646.

[18] Z. Rosenberg, On the relation between the hugoniot elastic limit and the yield strength of brittle materials, J. Appl. Phys. 74 (1993) 752–753.
[19] M.W. Chen, J.W. McCauley, D.P. Dandekar, K. Bourne, Dynamic plasticity and failure of high-purity alumina under shock loading, Nature 5 (2006) 614.
[20] M.A. Meyers, V.F. Nesterenko, J.C. LaSalvia, Q. Xue, Shear localization in dynamic deformation of materials: microstructural evolution and self-organization, Mater. Sci. Eng. C 317 (2001) 204–225.
[21] V.F. Nesterenko, M.A. Meyers, H.C. Chen, Shear localization in high-strain-rate deformation of granular alumina, Acta Mater. 44 (1996) 2017–2026.
[22] V.F. Nesterenko, M.A. Meyers, H.C. Chen, J.C. LaSalvia, Chemical reactions in controlled high-strain-rate shear bands, Proceedings of the conference of the American Physical Society topical group on shock compression of condensed matter, in: AIP Conference Proceedings 370, 1996, pp. 713–716.
[23] J. Akedo, M. Lebedev, Piezoelectric properties and poling effect of Pb (Zr, Ti) O 3 thick films prepared for microactuators by aerosol deposition, Appl. Phys. Lett. 77 (2000) 1710–1712.
[24] J. Akedo, M. Lebedev, Microstructure and electrical properties of lead zirconate titanate (Pb (Zr52/Ti48) O3) thick films deposited by aerosol deposition method, Jpn. J. Appl. Phys. 38 (1999) 5397.
[25] J. Akedo, Aerosol deposition of ceramic thick films at room temperature: densification mechanism of ceramic layers, J. Am. Ceram. Soc. 89 (2006) 1834–1839.
[26] J. Akedo, Room temperature impact consolidation (RTIC) of fine ceramic powder by aerosol deposition method and applications to microdevices, J. Therm. Spray Technol. 17 (2008) 181–198.
[27] J. Akedo, Aerosol deposition method for fabrication of nano crystal ceramic layer, Mater. Sci. Forum 43–48 (2004).
[28] D. Hanft, J. Exner, M. Schubert, T. Stöcker, P. Fuierer, R. Moos, An overview of the aerosol deposition method: process fundamentals and new trends in materials applications, J. Ceram. Sci. Technol. 6 (2015) 147–182.
[29] H. Assadi, F. Gärtner, T. Stoltenhoff, H. Kreye, Bonding mechanism in cold gas spraying, Acta Mater. 51 (2003) 4379–4394.
[30] K. Ma C. J. Li C. X. Li , Narrow and thin copper linear pattern deposited by vacuum cold spraying and deposition behavior simulation, J. Therm. Spray Technol., doi: 10.1007/s11666-020-01102-w.
[31] D.M. Chun, S.H. Ahn, Deposition mechanism of dry sprayed ceramic particles at room temperature using a nano-particle deposition system, Acta Mater. 59 (2011) 2693–2703.
[32] M. Yamada, N.T. Salim, H. Isago, K. Shima, H. Nakano, M. Fukumoto, The understanding on adhesion mechanism of cold sprayed TiO_2 coating, in: Proceeding of International Thermal Spray Coatings ITSC 2011, Hamburg, Germany, September 27 – 29, 2011.
[33] M. Yamada, M.E. Dickinson, K. Shima, N.T. Salim, H. Nakano, M. Fukumoto, Deposition behavior and adhesion strength of cold-sprayed TiO_2 particles, in: Proceeding of International Thermal Spray Coatings ITSC 2011, Hamburg, Germany, September 27 – 29, 2011.
[34] H. Gutzmann, I. Irkhin, F. Gärtner, T. Klassen, An experimental approach to gain insight into cold spraying of ceramics, in: Proceedings of the International Thermal Spray Conference, June 7-9, 2017, DVS Media GmbH, Curran Associates Inc., Dusseldorf, Germany, 2017, pp. 515–517.
[35] H. Ogawa, Molecular dynamics simulation on the single particle impacts in the aerosol deposition process, Mater. Trans. 46 (2005) 1235–1239.
[36] H. Ogawa , Atomistic simulation of the aerosol deposition method with zirconia nanoparticles, Mater. Trans., 47 (206) 1945 – 1948.
[37] H. Ogawa, Molecular dynamics simulation on the modification of crystallographic orientation in fragmented particles in the aerosol-deposition process, Mater. Trans. 48 (2007) 2067–2071.
[38] B. Daneshian, H. Assadi, Impact behavior of intrinsically brittle nanoparticles: a molecular dynamics perspective, J. Therm. Spray Technol. 23 (2014) 541–550.
[39] H. Park, J. Kim, C. Lee, Dynamic fragmentation process and fragment microstructure evolution of alumina particles in a vacuum kinetic spraying system, Scr. Mater. 108 (2015) 72–75.
[40] H. Park, J. Kwon, I. Lee, C. Lee, Shock-induced plasticity and fragmentation phenomena during alumina deposition in the vacuum kinetic spraying process, Scr. Mater. 100 (2015) 44–47.
[41] B. Daneshian, F. Gärtner, H. Assadi, D. Höche, W. Weber, T. Klassen, Size effects of brittle particles in aerosol deposition – molecular dynamics simulation, Therm. Spray Technol. (2021), https://doi.org/10.1007/s11666-020-01149-9.
[42] J. Nowotny, T. Bak, M.K. Nowotny, L.R. Sheppard, Titanium dioxide for solar-hydrogen I. Functional properties, Int. J. Hydrogen Energ. 32 (2007) 2609–2629.
[43] H. Zhang, J.F. Banfield, Structural characteristics and mechanical and thermodynamic properties of nanocrystalline TiO_2, Chemistry 114 (2014) 9613–9644.
[44] M.P. Allen, D.J. Tildesley, Computer Simulation of Liquids, Second Edition, Oxford University Press, Oxford, 2017, ISBN 9780198803195.
[45] S. Plimpton, Fast parallel algorithms for short-range molecular dynamics, J. Comput. Phys. 117 (1995) 1–19.
[46] A. Stukowski, Visualization and analysis of atomistic simulation data with OVITO–the open visualization tool, Model Simul. Mater. SC 18 (2009), 015012.
[47] F. Shimizu, S. Ogata, J. Li, Theory of shear banding in metallic glasses and molecular dynamics calculations, Mater. Trans. 48 (2007) 2923–2927.
[48] P.L. Williams, Y. Mishin, J.C. Hamilton, An embedded-atom potential for the Cu–Ag system, Model Simul. Mater. SC 14 (2006) 817.
[49] J. Wu, H. Fang, S. Yoon, H. Kim, C. Lee, The rebound phenomenon in kinetic spraying deposition, Scr. Mater. 54 (4) (2006) 665–669.
[50] R.W. Davidge, Mechanical properties of ceramic materials, Contemp. Phys. 10 (2) (1969) 105–124.
[51] H. Kwon, Y. Kim, H. Park, C, lee, impact behavior for successful particle-particle bonding in vacuum kinetic spraying, J. Therm. Spray Technol. (2020), https://doi.org/10.1007/s11666-020-01078-7.
[52] H. Assadi, H. Kreye, F. Gärtner, T. Klassen, Cold spraying – a materials perspective, Acta Mater. 116 (2016) 382–407.
[53] T. Klassen, F. Gärtner, H. Assadi, in: High Pressure Cold Spray: Principles and Applications, Process Science of Cold Spray, ASM International, New York, 2016, ISBN 978-1-62708-096-5, pp. 17–66.
[54] H. Assadi, F. Gärtner, T. Klassen, in: High Pressure Cold Spray: Principles and Applications, Modeling and Simulation of Cold Spray, ASM International, New York, 2016, ISBN 978-1-62708-096-5, pp. 67–106.
[55] H.J.C. Berendsen, J.P.M. Postma, W.F. van Gunsteren, A. DiNola, J.R. Haak, Molecular dynamics with coupling to an external bath, J. Chem. Phys. 81 (1984) 3684–3690.
[56] A. Carpinteri, A. Spagnoli, A fractal analysis of size effect on fatigue crack growth, Int. J. Fatigue 26 (2004) 125–133.
[57] B.B. Mandelbrot, D.E. Passoja, A.J. Paullay, Fractal character of fracture surfaces of metals, Nature 308 (1984) 721.
[58] M. Suzuki, T. Tsuchiya, J. Akedo, Effect of starting powder morphology on film texture for bismuth layer-structured ferroelectrics prepared by aerosol deposition method, Jpn. J. Appl. Phys. 56 (6S1) (2017) 06GH02.
[59] J. Exner, M. Schubert, D. Hanft, J. Kita, R. Moos, How to treat powders for the room temperature aerosol deposition method to avoid porous, low strength ceramic films, J. Eur. Ceram. 39 (2–3) (2019) 592–600.
[60] J. Exner, M. Hahn, M. Schubert, D. Hanft, P. Fuierer, R. Moos, Powder requirements for aerosol deposition of alumina films, Adv. Powder Technol. 26 (4) (2015) 1143–1151.
[61] J. Ryu, D.S. Park, B.D. Hahn, J.J. Choi, W.H. Yoon, K.Y. Kim, H.S. Yun, Photocatalytic TiO_2 thin films by aerosol-deposition: from micron-sized particles to nano-grained thin film at room temperature, Appl. Catal. B 83 (2008) 1–7.
[62] J. Ryu, B.D. Hahn, J.J. Choi, W.H. Yoon, B.K. Lee, J.H. Choi, D.S. Park, Porous photocatalytic TiO_2 thin films by aerosol deposition, J. Am. Ceram. Soc. 93 (2010) 55–58.
[63] J.G. Wang, Y.C. Hu, P.F. Guan, K.K. Song, L. Wang, G. Wang, Y. Pan, B. Sarac, J. Eckert, Hardening of shear band in metallic glass, Sci. Rep. 7076 (2017) 1–10.
[64] N. Djordjevic, R. Vignjevic, T. De Vuyst, S. Gemkow, J. Campbell, K. Hughes, Localization and damage induced softening using finite element and smooth particle hydrodynamic methods, JSSCM 11 (2017) 120–129.